UNLV | University Libraries
University of Nevada, Las Vegas

Physics & Astronomy Faculty Publications | Physics and Astronomy

7-14-2019

Topological Nodal Line Semimetals in Graphene Network Structures

Jian-Tao Wang
University of Chinese Academy of Sciences, wjt@aphy.iphy.ac.cn

Hongming Weng
University of Chinese Academy of Sciences

Chengfeng Chen
University of Nevada, Las Vegas, changfeng.chen@unlv.edu

Follow this and additional works at: https://digitalscholarship.unlv.edu/physastr_fac_articles

 Part of the Quantum Physics Commons

Repository Citation

Wang, J., Weng, H., Chen, C. (2019). Topological Nodal Line Semimetals in Graphene Network Structures. *Advances in Physics: X, 4*(1), 1-27. Taylor & Francis Open.
http://dx.doi.org/10.1080/23746149.2019.1625724

This Article is protected by copyright and/or related rights. It has been brought to you by Digital Scholarship@UNLV with permission from the rights-holder(s). You are free to use this Article in any way that is permitted by the copyright and related rights legislation that applies to your use. For other uses you need to obtain permission from the rights-holder(s) directly, unless additional rights are indicated by a Creative Commons license in the record and/or on the work itself.

This Article has been accepted for inclusion in Physics & Astronomy Faculty Publications by an authorized administrator of Digital Scholarship@UNLV. For more information, please contact digitalscholarship@unlv.edu.

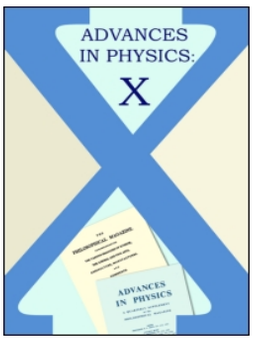

Advances in Physics: X

ISSN: (Print) 2374-6149 (Online) Journal homepage: https://www.tandfonline.com/loi/tapx20

Topological nodal line semimetals in graphene network structures

Jian-Tao Wang, Hongming Weng & Changfeng Chen

To cite this article: Jian-Tao Wang, Hongming Weng & Changfeng Chen (2019) Topological nodal line semimetals in graphene network structures, Advances in Physics: X, 4:1, 1625724, DOI: 10.1080/23746149.2019.1625724

To link to this article: https://doi.org/10.1080/23746149.2019.1625724

© 2019 The Author(s). Published by Informa UK Limited, trading as Taylor & Francis Group.

Published online: 14 Jul 2019.

Submit your article to this journal

Article views: 67

View Crossmark data

Full Terms & Conditions of access and use can be found at
https://www.tandfonline.com/action/journalInformation?journalCode=tapx20

ADVANCES IN PHYSICS: X
2019, VOL. 4, NO. 1, 1625724
https://doi.org/10.1080/23746149.2019.1625724

Taylor & Francis
Taylor & Francis Group

REVIEW ARTICLE

OPEN ACCESS Check for updates

Topological nodal line semimetals in graphene network structures

Jian-Tao Wang[a,b,c], Hongming Weng[a,b,c,d] and Changfeng Chen[e]

[a]Beijing National Laboratory for Condensed Matter Physics, Institute of Physics, Chinese Academy of Sciences, Beijing, China; [b]School of Physics, University of Chinese Academy of Sciences, Beijing, China; [c]Songshan Lake Materials Laboratory, Dongguan, Guangdong, China; [d]CAS Center for Excellence in Topological Quantum Computation, University of Chinese Academy of Sciences, Beijing, China; [e]Department of Physics and Astronomy, University of Nevada, Las Vegas, NV, USA

ABSTRACT

Topological semimetals are a fascinating class of quantum materials that possess extraordinary electronic and transport properties. These materials have attracted great interests in recent years for their fundamental significance and potential device applications. There have been intensive studies suggested that three-dimensional graphene networks support topological semimetals with two types of continuous nodal lines: one is to form closed nodal rings in Brillouin zone and the other ones traversing the whole Brillouin zone to be periodically connected. Carbon has negligible spin-orbit coupling, non-magnetism and great diversity of allotropes, which makes it very promising in realizing topological nodal line semimetals. Here we review recent efforts in proposing various carbon allotropes to realize these two types of nodal line semimetals. The nodal rings or lines are protected by the coexistence of time reversal and spatial inversion symmetries. When projecting these nodal lines or rings onto the certain surface, drumhead like surface flat bands will appear. Based on these flat bands, Chern insulator and high-temperature superconductor will be induced by electron-electron correlation effects. The recent discoveries of Mott insulator and superconductor in twisted bilayer graphene-related with flat bands have made these reviewed efforts very important and meaningful.

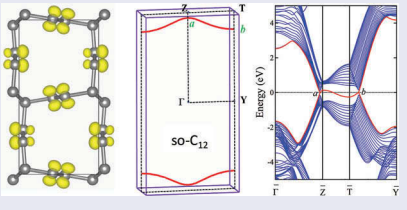

ARTICLE HISTORY
Received 17 April 2019
Accepted 19 May 2019

KEYWORDS
Carbon; nodal line semimetal; *Ab initio* calculations

CONTACT Jian-Tao Wang wjt@aphy.iphy.ac.cn Beijing National Laboratory for Condensed Matter Physics, Institute of Physics, Chinese Academy of Sciences, Beijing, China

© 2019 The Author(s). Published by Informa UK Limited, trading as Taylor & Francis Group.
This is an Open Access article distributed under the terms of the Creative Commons Attribution-NonCommercial License (http://creativecommons.org/licenses/by-nc/4.0/), which permits unrestricted non-commercial use, distribution, and reproduction in any medium, provided the original work is properly cited.

1. Introduction

Carbon exhibits an extremely rich variety of allotropic forms [1] that possess a wide range of properties with numerous applications in many areas of science and technology. Despite the existence of a large number of known carbon allotropes, the quest for new carbon structures has been a very active research field. The valence electrons of the carbon atom are capable of forming sp^3-, sp^2-, and sp^1-hybridized states that support four basic types of single, double, triple, and aromatic C-C bonds, which are closely related to the bonding configurations in ethane, ethene, ethyne, and benzene-type hydrocarbon structures [2–6]. At ambient conditions, graphite, which is structurally related to polycyclic benzenoid aromatic hydrocarbon, is the most thermodynamically stable carbon configuration. The polycyclic carbon atoms form a two-dimensional three-connected benzenoid sp^2 bonding network with bond angles of 120^o and bond lengths of 0.142 nm. Diamond, which is related to polycyclic-saturated hydrocarbon, is the second most stable allotrope of carbon with all the carbon atoms in a methane-like tetrahedral sp^3 bonding with bond angles of 109.47^o and bond lengths of 0.1544 nm as in alkanes, forming a very rigid three-dimensional four-connected carbon network with a larger band gap of 5.47 eV [4]. Under static pressure, the highly crystalline varieties of graphite can be transformed to diamond via slipping, buckling, and cross-linking of the carbon sheets with an $sp^2 \rightarrow sp^3$ bonding transition [7–16]. Moreover, a rich variety of carbon phases have been synthesized under laboratory conditions, including, most notably, carbon nanotubes [17], fullerenes [18], graphene [19], graphyne (or graphdiyne) [20–24], and the simplest polyyne-like carbyne chains [5].

In addition to these well-characterized carbon allotropes, a new type of stable chiral framework structures comprising threefold, fourfold [2] and sixfold [6] helical chains have been identified in all-sp^2 bonding networks connected by ethene-type planar π conjugation. By inserting acetylenic or diacetylenic bonds into the all sp^2-hybridized polybenzene lattice, the three-dimensional (3D) polybenzene-ynes in $sp + sp^2$ hybridized bonds with phenylic rings and acetylenic chains have been reported [25]. Also, 3D sp+sp^3-yne-diamond was suggested by inserting acetylenic linkers into the C-C bonds in cubic diamond and supercubane [26–29]. Meanwhile, a family of hypothetical graphitic foams with mixed sp^2-sp^3 hybridized bonding networks have been proposed theoretically [30–32] and investigated in experiments [33–36] by inserting a phenyl ring into each C-C bond of the diamond lattice.

Topological semimetals are a fascinating class of quantum materials that possess extraordinary electronic and transport properties [37–57]. These materials have attracted great interest in recent years for their fundamental significance and potential device applications. In this paper, we review the topological semimetals found in 3D graphene network structures [58–68]. According to the classification of

topological nodal-line semimetals suggested by Hyart *et al.* [69], topological semimetals in 3D graphene networks can be divided into two types: type A has closed nodal rings in the Brillouin zone (BZ), while type B has continuous nodal lines that traverse the whole BZ to be periodically connected. The topological semimetals with nodal rings have been found in all-sp^2 carbon network structures such as Mackay-Terrones carbon crystal [59], body-centered orthorhombic C_{16} [62], and body-centered tetragonal C_{16} [64]; meanwhile, the topological semimetals with nodal lines have been found in sp^2-sp^3 hybrid network structures such as interpenetrated graphene network C_6 [60], orthorhombic C_{24} [65], monoclinic mC_{16} [66], simple orthorhombic C_{12} [67], and body-centered tetragonal C_{40} [68]. These topological nodal lines or nodal rings are protected by the coexistence of time reversal and spatial inversion symmetry in bulk and form drumhead-like surface flat bands either inside or outside of the nodal lines when the nodal lines are projected onto certain surfaces.

2. Nodal points in 2D graphene and graphyne sheets

To get the best understanding on the electronic property of 3D graphene network structures, we first introduce the typical electronic property of graphene. As a typical example of topological semimetal of carbon, graphene [70] possesses more superior comprehensive properties, such as high thermal conductivity [71], high strength [72], high chemistry stability [73], and giant intrinsic charge mobility [74]. The electronic property of graphene can be described by a Dirac-like equation, $H = v\vec{k} \cdot \vec{\sigma}$, where v is the velocity, $\vec{k} = (k_x, k_y)$ is the momentum, and $\vec{\sigma}$ is the Pauli matrix [75]. In the 2D BZ, the valence and conduction bands meet in a single point K at the Fermi level [see Figure 1(a)] and yield a Dirac cone [see Figure 1(b)]. Around Dirac points the valence and conduction bands exhibit a linear dispersion. To protect the 2D Dirac cone, two conditions are required: (i) the absence of spin-orbit coupling (SOC) and (ii) the presence of inversion symmetry. The first condition is naturally satisfied in graphene, because its SOC strength is negligible small (10^{-3} meV). The second requirement is satisfied in the presence of A-B sublattice symmetry in the honeycomb structure [75]. The similar Dirac cone is also found in the honeycomb-like α-graphyne structure [76]. The hexagonal lattice symmetry (*p6m*) like graphene is commonly considered a necessary precondition for the presence of Dirac cones. However, the existence of Dirac cone-like features in the band structure of 2D materials does neither depend on a honeycomb structure nor on hexagonal symmetry [76]. One of these materials, 6,6,12-graphyne, has a rectangular (*pmm*) [see Figure 1(c)] instead of a hexagonal symmetry and exhibits two distorted Dirac points along the G-Y and S-X direction [see

Figure 1(d)] in its 2D BZ. Such 2D graphene and graphyne sheets with one or two Dirac point are characterized as a nodal-point semimetal [37]. When the dimension is extended from 2D to 3D, the Dirac point at *K*-point in graphene has been found to be kept along the *z*-direction to form a nodal line near the *H*-*K*-*H* edge in the hexagonal BZ of graphite [58].

3. Nodal rings in all-sp^2 3D carbon network structures

In this section, we introduce two type-A topological nodal line semimetals found in all-sp^2 Mackay-Terrones carbon crystal [59] and body-centered orthorhombic C_{16} [62].

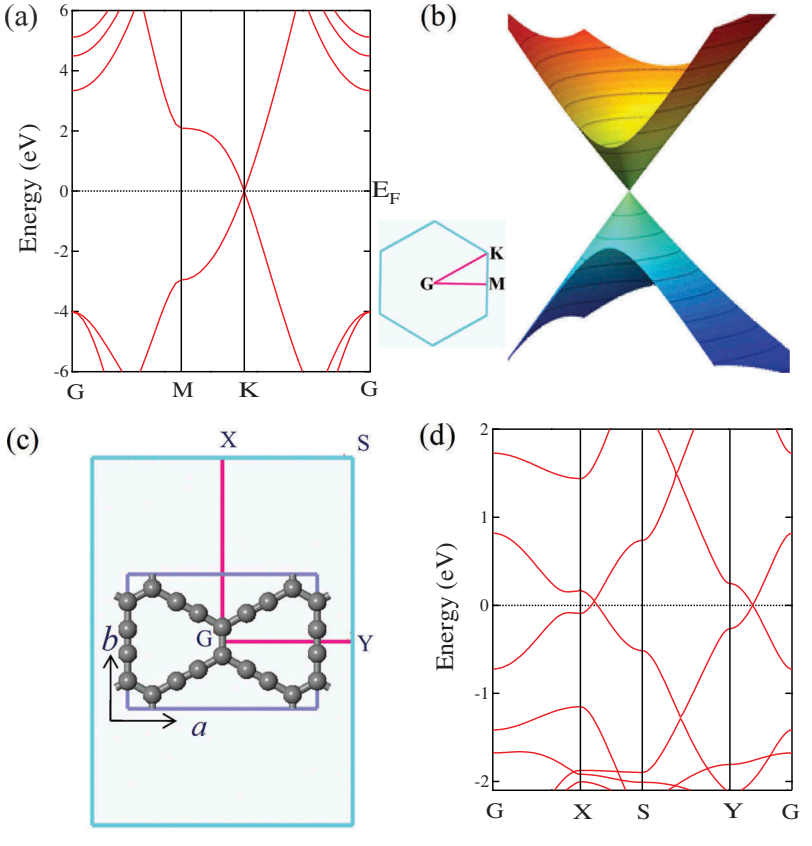

Figure 1. (a) Electronic band structure of 2D graphene along several high-symmetry directions of G-M-K-G. (b) Dirac cone formed by the valence and conduction band in the vicinity of the Dirac point *K*. (c) Rectangular 6,6,12-graphyne in *pmm* symmetry with lattice parameters a = 9.4980 Å, b = 6.7323 Å, and its 2D BZ. (d) Electronic band structure of 2D 6,6,12-graphyne along with the high-symmetry directions of G-X-S-Y-G.

3.1. Nodal rings in cubic mackay-terrones crystal

Based on first-principles calculations and tight-binding (TB) analyses, Weng *et al.* [59] have predicted that a family of all-carbon 3D allotrope, Mackay-Terrones crystals, can have topological node-line semimetal state that has three nodal rings, protected by both time reversal and spacial inversion symmetry.

Figure 2(a) shows a cubic symmetric Mackay-Terrones crystal (MTC) of carbon. It comprises a characteristic all-sp^2 six-membered-ring bonding network with a 176 atom unit cell in $Pm\bar{3}m$ (O_h^1, No. 221) symmetry [77]. The lattice parameters are estimated to be $a =$ 14.557 Å, occupying six nonequivalent atomic Wyckoff positions of 8*g* (0.2279, 0.2279, 0.2279), 24*m* (0.1864, 0.1864, 0.3073), 24*m* (0.2809, 0.0492, 0.2809), 24*l* (0.1591, 0.0928, 0.5), 48*n* (0.2178, 0.0979, 0.3367), and 48*n* (0.1879, 0.0480, 0.4156). The bond

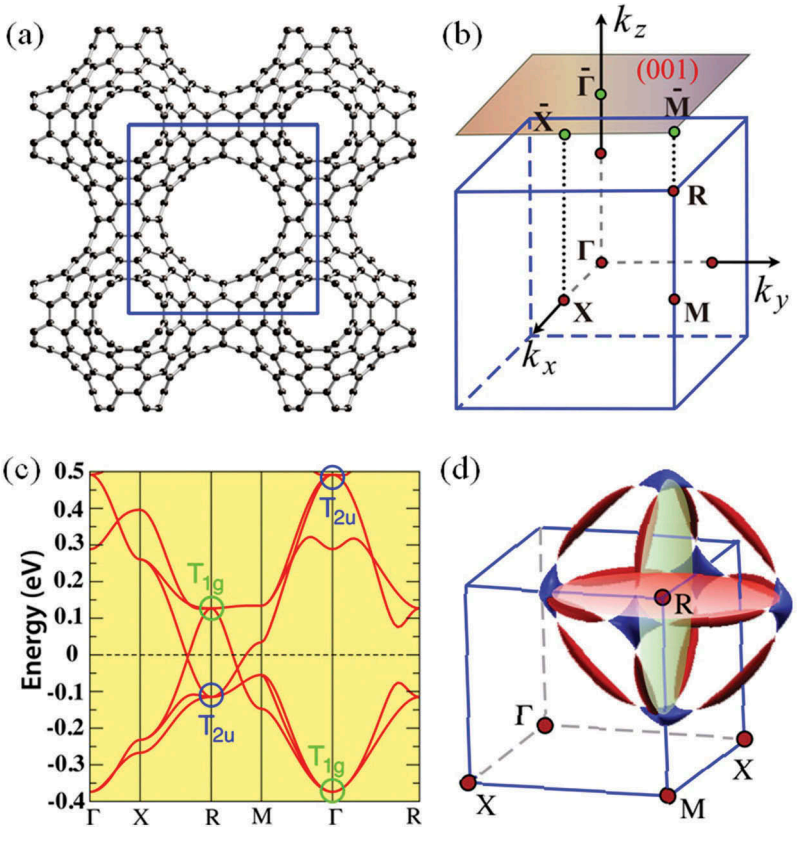

Figure 2. (a) Schematic depiction of the structure of MTC. (b) Bulk and (001)-surface BZ, as well as the highly symmetrical *k* points. (c) Band structure from the first-principles calculation. The two triply degenerate eigenstates at Γ and R with T_{1g} and T_{2u} symmetrical representation are marked. The band inversion between them can be easily seen. (d) The Fermi surface consists of three lotus-root-like rings from the tight-binding calculation. These rings are center the R point and are parallel to the $k_x = \pi a$, $k_y = \pi a$, and $k_z = \pi a$ plane, respectively. They are formed by the electron pockets (blue) and hole pockets (red) connected by nodal points at the Fermi energy.

lengths are between $1.36-1.44$ Å, which are on average close to 1.42 Å in graphene. Detailed analysis of the band structure reveals the following: (i) The occupied and unoccupied low-energy bands [see Figure 2(b,c)] are triply degenerate at Γ, and they have T_{1g} and T_{2u} symmetry, respectively. Those of T_{1g} are even while those of T_{2u} are odd under spatial inversion symmetry. Moving away from the Γ point their degeneracy is lifted, but upon arriving at the R point their degeneracy is recovered again. However, their energy ordering exchanges, leading to the so-called band inversion, which is one of the key ingredients for the topological insulators [78]. Due to the band inversion, the band crossings happen along both X-R and R-M paths, as seen from Figure 2(c); (ii) Including SOC in the first-principles calculation, a gap will open up around the band crossings, leading to a 3D strong topological insulator. However, similar to graphene, the computed SOC splitting is small (around 0.13 meV or 1.5 K), and it can be neglected in cases with a temperature higher than 1.5 K. Moreover, the detailed tight-binding analyses show that the band crossings exist along certain-closed loops in 3D BZ, and they generate three ring-like nodal lines around the R point [see Figure 2(d)]. These nodal rings are protected by the coexistence of time reversal (T) and spacial inversion (P) symmetry.

With the coexistence of P and T symmetries, there exists a certain gauge choice under which the spineless Hamiltonian is completely real-valued [59]. For this system, if there is an energy level-crossing of two bands at a momentum $\mathbf{k}_0$, a stable node-line will unavoidably appear. Around the crossing point, the two-level 2×2 Hamiltonian can be written in the following general form:

$$\mathcal{H} = d_0(\vec{k}) + d_x(\vec{k})\cdot\sigma_x + d_y(\vec{k})\cdot\sigma_y + d_z(\vec{k})\cdot\sigma_z, \tag{1}$$

where the Pauli matrices σ_i $(i = x, y, z)$ denote the two-band space. Without loss of generality, $d_i(\vec{k})(i = 0, x, y, z)$ are all real function of $\vec{k}$. The eigen energy of $\mathcal{H}$ being

$$E(\vec{k}) = \pm\sqrt{d_x^2(\vec{k}) + d_y^2(\vec{k}) + d_z^2(\vec{k})} + d_0(\vec{k}), \tag{2}$$

and the energy degeneracy can be obtained when the three conditions $d_i(\vec{k}) = 0$ $(i = x, y, z)$ are satisfied with three parameters $\vec{k}(k_x, k_y, k_z)$ in the 3D momentum space. As mentioned above, the Hamiltonian can be chosen to be real-valued leading to $d_y = 0$. The rest $d_0(\vec{k})$, $d_x(\vec{k})$ and $d_z(\vec{k})$ can be expanded around k_0 and the location of the crossing points can be determined by $d_x(\vec{k}_0) \approx \delta_x + \vec{v}_x(\vec{k} - k_0) = 0$ and $d_z(\vec{k}_0) \approx \delta_z + \vec{v}_z(\vec{k} - k_0) = 0$, where $\vec{v}_i = \vec{\nabla}_{\vec{k}} d_i(\vec{k})$ and δ_i denote the small perturbative terms with both T and P symmetries. In the generic case, the above two equations give a line in the vicinity of k_0

with its direction determined by $\vec{v}_x \times \vec{v}_z$. Therefore, the generic solution of the band crossing point in 3D k-space is a closed rings. Any external perturbations that keep T, P and translational symmetry can only shift or distort but not eliminate the nodal rings.

Since the two crossing bands have opposite mirror eigenvalue when they are in the mirror plane of k_z (or k_x,k_y) $= \pi a$, the topologically stable nodal line in MTC can be looked as to be protected by P and T or by the mirror symmetry of the above planes. The cubic symmetry leads to three in-plane nodal rings, as was found from the tight-binding calculations in Figure 2 (d). The nodal rings are not necessarily flat in energy, and they can have energy dispersion in the k space determined by the $d_0(\mathbf{k})$ term (which breaks the particle-hole symmetry). The situation becomes even more interesting if P symmetry is broken further. In such a case, from the above discussions, we will generally expect three conditions $d_0(\mathbf{k}) = 0$ with three parameters for the band crossing points, leading to isolated points in the 3D k space. In fact, although the calculated perfect structure has inversion symmetry, most of the known real samples of MTC have strong defects and orientation disorder, which should break inversion symmetry. The plausible existence of these stable 3D Dirac points has been indicated by the density of states [79].

Such topologically stable node-line semimetal state can have nontrivial surface states. For the (001) surface, the three node-line rings are projected to be a ring and two orthogonal diameter segments inside of it, as shown in Figure 3(a). The (001) surface state is calculated based on the six-band TB model using both the Green's function method and the slab-model method. There is a nearly flat surface band nestled inside of the projected node-line ring with its bandwidth being about 40 meV due to the particle-hole asymmetry. The peak-like surface density of states contributed by this nearly flat band is clearly shown in Figure 3(b), which is proposed to be an important route to high-temperature surface superconductivity [80]. The layer-resolved weight of the wave function for the surface flat band is shown in Figure 3(c). It penetrates just three layers into the bulk with most of the weight on the surface layer. The surface localization of these flat bands is well resolved for those separated from bulk bands. The nestled flat surface states have small dispersion, and their eigenenergy distribution in the surface BZ is shown in Figure 3(d), which looks like some vibrational mode of a drumhead. Such drumhead-like states are readily detected by angle-resolved photoelectron spectroscopy or scanning tunneling microscopy [49].

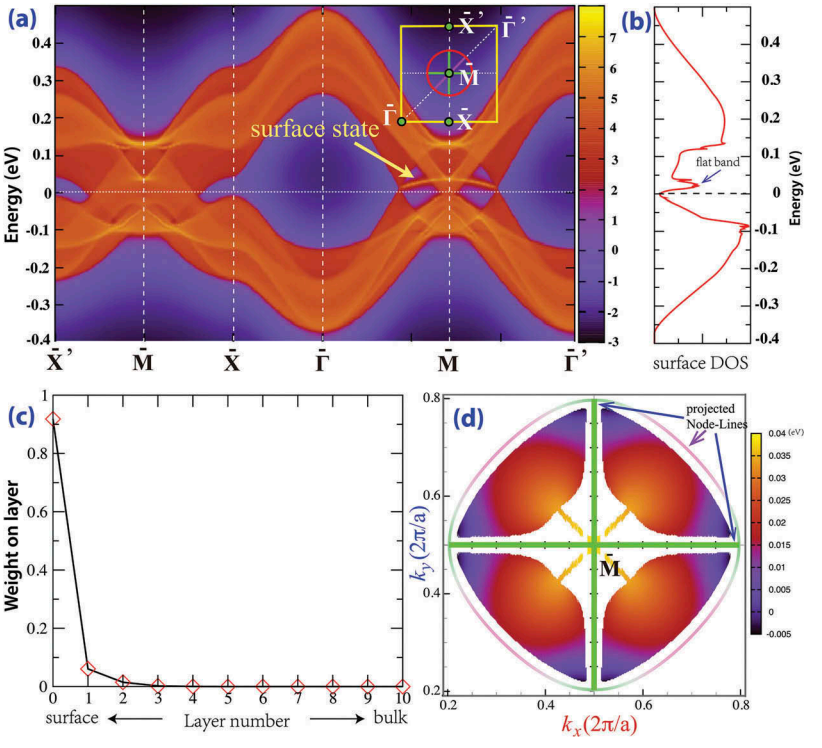

Figure 3. The (001)-surface state of MTC. (a) The nearly flat surface band is nestled between two solid Dirac cones, which are the projection of one of the node-line circles as indicated in the inset (red circle). The other two node-line rings are projected as two orthogonal diameters (green line). (b) The surface density of state. (c) The wave function of the surface state indicated by the arrow decays rapidly into bulk. (d) The eigenenergy distribution of a surface flat band nestled inside of a projected node-line circle, which looks like a vibration model of a *drumhead*. The mixing of surface and bulk states leads to discontinuity in this plot.

3.2. Nodal ring in body-centered orthorhombic C_{16}

Distinct from the cubic symmetric MTC that has three nodal rings in its bulk BZ [59], Wang *et al.* reported a new type of nodal line semimetal that has one nodal ring in body-centered orthorhombic C_{16} (termed bco-C_{16}) [62].

The bco-C_{16} carbon has a 16-atom body-centered orthorhombic unit cell in *Imma* (D_{2h}^{28}, No. 74) symmetry [see Figure 4(a)]. The lattice parameters are estimated to be a = 7.8061 Å, b = 4.8772 Å, and c = 3.2372 Å with the carbon atoms occupying two nonequivalent atomic Wyckoff positions of 8i (0.3231, 0.25, 0.1258) and 8f (0.0885, 0.5, 0.5), denoted by C_1 and C_2, respectively. This structure topologically corresponds to a 2D ($2\sqrt{3} \times 2$) graphene-like lattice with one-third double and two-thirds single C-C bonds. Therefore, it also can be regarded as a 3D modification of graphite in AA stacking consisting of benzene linear chains connected by ethene-type planar π-conjugation. However, in contrast to the uniform bond length of 1.42 Å in graphite, there are three distinct C-C bond lengths, a longer bond of 1.459 Å (d_1) associated with a butadiene-

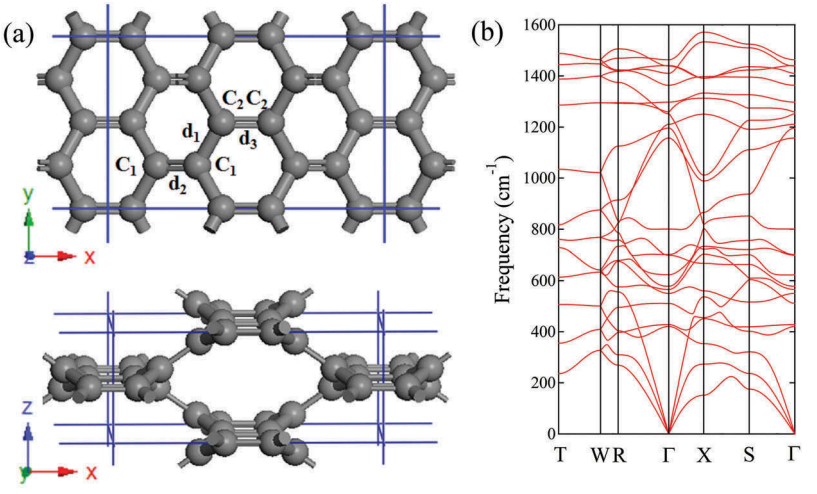

Figure 4. Structure of bco-C_{16} and its phonon dispersion. (a) Top and side view of the all-sp^2 bco-C_{16} in *Immma* (D_{2h}^{28}) symmetry with one-third double (d_2, d_3) and two-thirds single (d_1) C-C bonds. It has a 16-atom body-centered orthorhombic structure with lattice parameters $a = 7.8061$ Å, $b = 4.8772$ Å, $c = 3.2372$ Å, occupying the 8*i* (0.3231, 0.25, 0.1258) and 8*f* (0.0885, 0.5, 0.5) Wyckoff positions, denoted by C_1 and C_2, respectively. (b) Calculated phonon dispersion curves of bco-C_{16} at zero pressure.

type $C_1(sp^2) - C_2(sp^2)$ single bond and two shorter bonds of 1.396 Å (d_2) and 1.382 Å (d_3) associated with ethene-type planar $C_1(sp^2) = C_1(sp^2)$ and $C_2(sp^2) = C_2(sp^2)$ double bonds, respectively. There are also three different bond angles, $\angle C_1 = C_1 - C_2 = 123.19^o$ out of the benzene rings, $\angle C_2 - C_1 - C_2 = 113.38^o$ and $\angle C_1 - C_2 = C_2 = 118.23^o$ in the benzene rings. Figure 4(b) shows the calculated the phonon dispersion of bco-C_{16}, no imaginary frequency in the entire BZ, confirming its dynamical stability.

Figure 5 present the calculated bulk and surface band structures of bco-C_{16} at equilibrium lattice parameters. It is shown that the valence and conduction bands of bco-C_{16} exhibit linear dispersion near the Fermi energy and cross at the Fermi level along the Γ-R direction [see Figure 5(a)], and further analysis of the band structure in the full BZ indicates that the band crossing points (or nodal points) of the valence and conduction bands in bco-C_{16} form a continuous nodal ring inside a mirror plane [the shaded region in Figure 5(b)]. Moreover, the states near the crossing points around the nodal ring are formed by the inversion of the valence and conduction bands and protected by the coexistence of the time-reversal and inversion symmetry. These electronic properties characterize bco-C_{16} as a topological node-line semimetal. When the nodal ring is projected onto the (100) surface, it produces topologically protected surface flat bands either inside or outside of the ring, depending on the termination of the surface, as shown in Figure 5(c,d). The SOC may open up a gap at the band crossing points, but the SOC in bco-C_{16}, estimated to be 0.74 meV, is negligibly

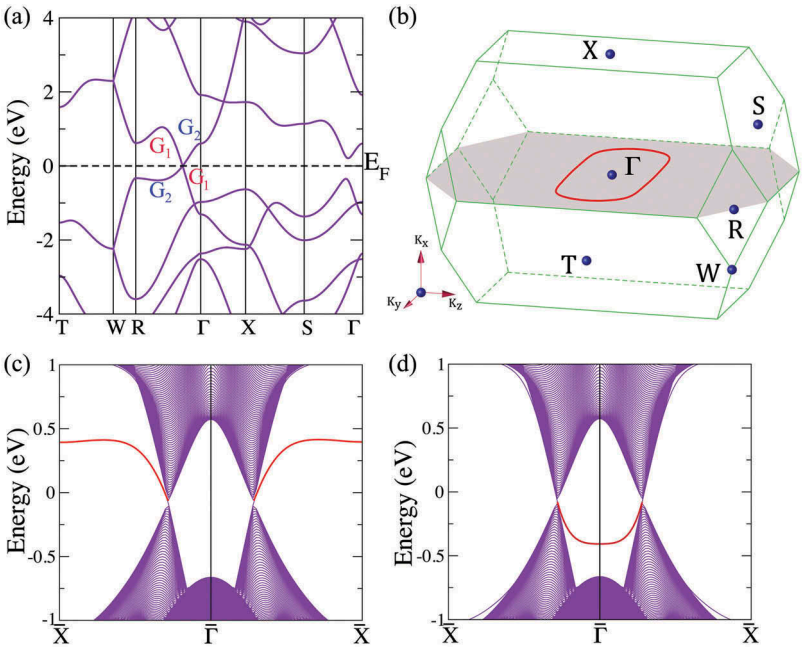

Figure 5. Calculated bulk and surface band structures of bco-C_{16} at equilibrium lattice parameters. (a) The bulk band structure along several high-symmetry directions. G_1 and G_2 indicate the irreducible representation of the two crossing bands, respectively. (b) The BZ with several high-symmetry momenta indicated. The nodal ring (red circle), formed by the band crossing points, is in the shaded mirror plane. (c) and (d) show the surface states for different zigzag-like (c) and beard-like (d) terminations of the (100) surface. The surface flat band (red line) can be outside or inside the surface-projected nodal ring.

weak at all but extremely low temperatures, thus not expected to alter the semimetal phase.

To establish the experimental connection of bco-C_{16}, we compare its simulated x-ray diffraction (XRD) spectra, along with those of graphite, diamond, rh6 [6], cT8 [2], cR6 [2], fcc-C_{60} [81], to the experimental data from detonation soot of TNT/diesel oil [82] and chimney soot [83] as shown in Figure 6. The measured XRD spectra reveals a considerable amount of amorphous carbon and provide clear evidence for several crystalline phases in the recovered specimen. The prominent peak around 26.5^o is attributed to the graphite (002) diffraction, and the weak peak around 43.7^o, matching that of the diamond (111) diffraction, indicates the presence of a small amount of cubic diamond. The most distinct feature of the measured XRD spectra is a strong peak at 30^o that does not match any previously known carbon phases [82–84]; the high intensity and sharpness of this peak along with its consistent presence in different experiments suggest that a new crystalline carbon phase has been produced. Our simulated XRD results show that the main (101) diffraction peak of bco-C_{16} perfectly matches this previously unexplained peak. It is noted that

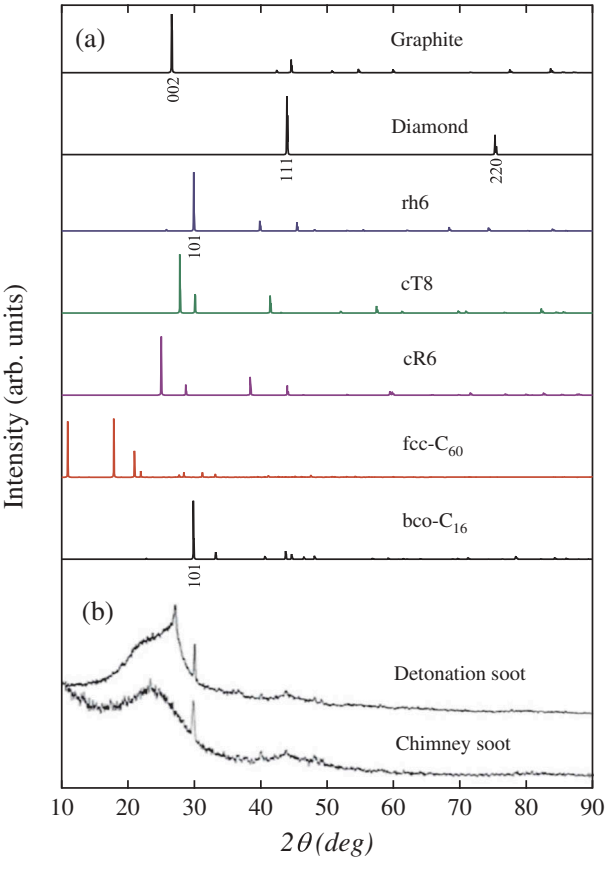

Figure 6. X-ray diffraction (XRD) patterns. (a) Simulated XRD patterns for graphite, diamond, rh6, cT8, cR6, fcc-C_{60}, and bco-C_{16}. (b) Experimental XRD patterns for detonation soot of TNT/diesel oil [82] and chimney soot [83]. X-ray wavelength is 1.5406 Å with a copper source.

the main peak of rh6 carbon is also close to 30^o because it also comprises sixfold helices (or benzene rings) [6], but bco-C_{16} is energetically more stable with a substantial energy gain of 0.12 eV per carbon atom [62] (see Figure 13) due to its complementary chirality. These structural and energetic results suggest that bco-C_{16} is a likely candidate of the intriguing new carbon phase observed in the detonation and chimney soot [82–84].

Similar nodal ring was also reported by Cheng *et al.* [64] in an all-sp^2 body-centered tetragonal C_{16}. This new carbon phase has a 16-atom unit cell in $I4_1/amd$ symmetry with space group No. 141, thus termed bct-C_{16}. It is consisting of two eightfold handed chains with same chirality, topologically corresponding to the 2D square lattice-like as cT8 [2], but less stable than cT8 (see Figure 13) with two fourfold left-handed and two fourfold right-handed chains connected by ethene-type π-conjugation. Due to the tetragonal symmetry, there is only one nodal ring in the BZ of bct-C_{16} like as that in bco-C_{16} [62], but distinct from the cubic symmetric MTCs [59] that has three nodal ring in

the bulk BZ. Note that the tetragonal symmetric sp^2-sp^3 hybrid carbon network structures favor to form a nodal-net [68] as shown in the following section.

4. Nodal lines in sp^2-sp^3 hybrid 3D carbon network structures

The type-B topological nodal line semimetal was firstly found in the interpenetrated graphene network C_6 (termed ign-C_6) [60]. Electronic band calculations revealed that ign-C_6 is a topological node-line semimetal with two mirror-inversion symmetric nodal lines that go through the whole BZ in bulk and a projected surface flat band around the Fermi level. Similar electronic property was also found in orthorhombic oC_{24} [65] and monoclinic mC_{16} [66]. Here we introduce two typical carbon network structures, a simple orthorhombic C_{12} [67] which has two mirror-inversion symmetric nodal lines as well as ign-C_6 and a body-centered tetragonal C_{40} [68] which has two mirror-inversion symmetric nodal nets consisting of multiple nodal lines in its bulk BZ.

4.1. Nodal lines in the simple orthorhombic C_{12}

The simple orthorhombic C_{12} phase contains 12 atoms in its unit cell, thus termed so-C_{12}. It can be constructed by inserting zigzag carbon chains between the graphene layers in AA stacking along the x direction or AB stacking along the y direction [see Figure 7(a)]. The calculated equilibrium lattice parameters are a = 4.313 Å, b = 8.604 Å, and c = 2.461 Å, occupying the $4d_1$ (0.0507, 0.2104, 0.25), $4d_2$ (0.0763, 0.0351, 0.25), and $4d_3$ (0.5783, 0.5052, 0.25) Wyckoff positions denoted by C_1, C_2 and C_3, respectively. The carbon

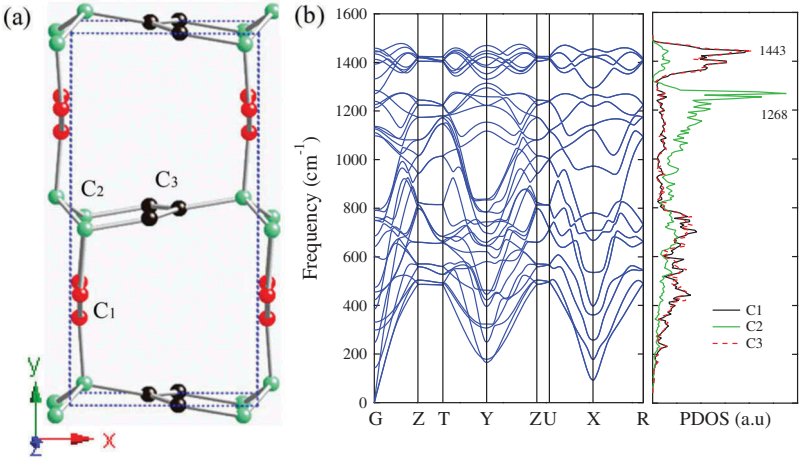

Figure 7. (a) The crystal structure of so-C_{12} in *Pbcm* (D_{2h}^{11}) symmetry with lattice parameters a = 4.313 Å, b = 8.604 Å, and c = 2.461 Å, occupying the $4d_1$ (0.0507, 0.2104, 0.25), $4d_2$ (0.0763, 0.0351, 0.25), and $4d_3$ (0.5783, 0.5052, 0.25) Wyckoff positions denoted by C_1, C_2 and C_3, respectively. (b) Phonon band structures and partial density of states (PDOS) for so-C_{12}. The peaks around 1443 cm^{-1} and 1268 cm^{-1} are related to sp^2 and sp^3 bonding, respectively.

atoms on the $4d_1$ and $4d_3$ sites form four zigzag carbon chains with aromatic sp^2 hybridization, while the carbon atoms on the $4d_2$ sites form two zigzag carbon chains with diamond-like sp^3 hybridization. Thus, there are three sets of distinct carbon-carbon bonds in this structure, namely two sp^3 single longer bonds of 1.512 Å (C_2-C_3 and C_2-C_1) and 1.520 Å (C_2-C_2), and a shorter sp^2 aromatic bond of 1.406 Å (C_1-C_1 and C_3-C_3). There are also two sets of distinct bond angles: 108.04^o for $\angle C_2$-C_2-C_2, 111.38^o for $\angle C_2$-C_2-C_1, and 111.04^o for $\angle C_2$-C_2-C_3, which are on average close to the 109.5^o angle in diamond; 118.95^o for $\angle C_2$-C_3-C_3, 118.90^o for $\angle C_2$-C_1-C_1, and 122.05^o for $\angle C_3$-C_3-C_3, which are on average close to the 120^o angle in graphene.

To assess the dynamical stability, we have calculated phonon dispersion and partial density of states (PDOS), and the obtained results are shown in Figure 7 (b). It is seen that there are two main peaks around 1443 cm^{-1} and 1268 cm^{-1} in the PDOS. The peak around 1443 cm^{-1} is related to the C_1 and C_3 carbon atoms in sp^2 bonding similar to the finding in all-sp^2 bco-C_{16} [62], while the peak around 1268 cm^{-1} is related to the C_2 carbon atoms in sp^3 bonding similar to the finding in diamond [85]. There are also some peaks below 800 cm^{-1} related to the C_1, C_2, and C_3 carbon atoms in sp^2-sp^3 hybrid bonds. No imaginary frequency exists in the entire BZ and PDOS, confirming the dynamical stability of so-C_{12}.

It is noted that so-C_{12} can be produced by a crystalline modification of (3,3) CNT. A double cell reconstruction pathway from polymeric (3,3) CNT [86,87] toward so-C_{12} is showed in Figure 8(a) and the enthalpy

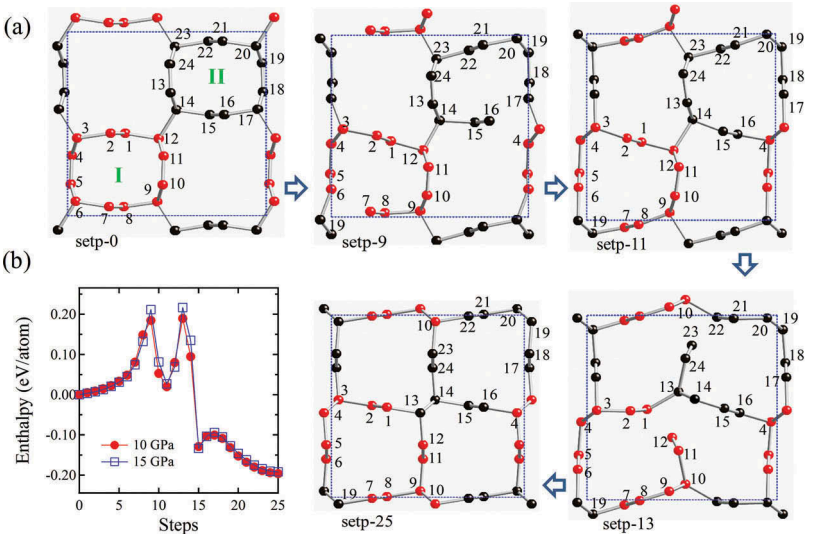

Figure 8. (a) A double cell reconstruction pathway from polymeric (3,3) CNT toward so-C_{12} with bond breaking between atoms 6–7 and 16–17 at step-9 and between atoms 1–12 and 22–23 at step-13. The atoms are marked as red in tube-I and black in tube-II, respectively. (b) Enthalpy versus pathway from polymeric (3,3) CNT toward so-C_{12} at 10 and 15 GPa.

versus pathway is plotted in Figure 8(b) at 10 and 15 GPa. There are two sharp enthalpy peaks in Figure 8(b). The first peak corresponds to the bond breaking between atoms 6–7 and 16–17 at step-9, followed by the enthalpy decrease with the rebonding between atoms 7–19 and 16–4 around step-11; the second peak corresponds to the bond breaking between atoms 1–12 and 22–23 at step-13, followed by the rebonding with atoms 12–13 and 10–23 with the bond rotation of atoms 13–14 and 9–10, respectively, to form the final so-C_{12} structure. Throughout this *bond rotation assisted* two-stage reconstruction pathway, the enthalpy barriers are estimated to be $0.19 - 0.22$ eV [see Figure 8(b)], which is similar to the findings in cold-compressed graphite phase transformations [11].

Figure 9(a) shows the calculated bulk band structure at equilibrium lattice parameters. It is seen that the valence and conduction bands exhibit linear dispersion near the Fermi energy and cross at the Fermi level to form several nodal points along with the high symmetric directions of G-Z, T-Y, and Y-Z in the bulk BZ. Further analysis of the band structure in the full BZ indicates that the band crossing points of the valence and conduction bands in so-C_{12} form two discrete *saddle* nodal lines inside a mirror plane G-Z-T-Y [see Figure 9(b)] with an inversion symmetry about the center of G in the bulk BZ. The states near the crossing points around the nodal lines are formed by the inversion of the valence and conduction bands. To clarify this point, we have calculated the band decomposed charge density near the nodal point b on the high symmetric direction T-Y in BZ [see Figure 9(c)]. One can see that the charge around the nodal points near the Fermi level are located on the C_1 and C_3 atoms and show the π-band character related to the p orbitals. The charge distributions for b_1 (and b_4) are 53.3% from C_1-p_x and 45.1% from C_3-p_y, while for b_2 (and b_3) the values are 49.3% from C_1-p_x and 49.3% from C_3-p_y orbitals. The obvious difference between the charge distributions of $b_1(b_4)$ and $b_2(b_3)$ reveal that the inversion of the valence and conduction bands on both the left and right side of the nodal point. This band inversion can be described by two crossing π bands of G_1 and G_2 throughout the full BZ around the nodal lines. Furthermore, these node lines are protected by the coexistence of time reversal (T) and spatial inversion (P) symmetry [59].

Figure 9(d,e) show the surface band structures calculated using a ten-layer thick slab geometry along the [010] crystalline direction [see Figure 9(f)]. The surface dangling bonds in Figure 9(e) are saturated with hydrogen atoms. The projected surface BZ $\bar{G}$-$\bar{Z}$-$\bar{T}$-$\bar{Y}$ is marked corresponding to G-Z-T-Y in bulk as shown in Figure 9(b). It is seen that when the resulted nodal lines are projected onto the surface BZ, they can produce one topologically protected surface flat band around the Fermi level, either outside [region containing the BZ boundaries in Figure 9(e)] or inside [region containing the $\bar{G}$ point in

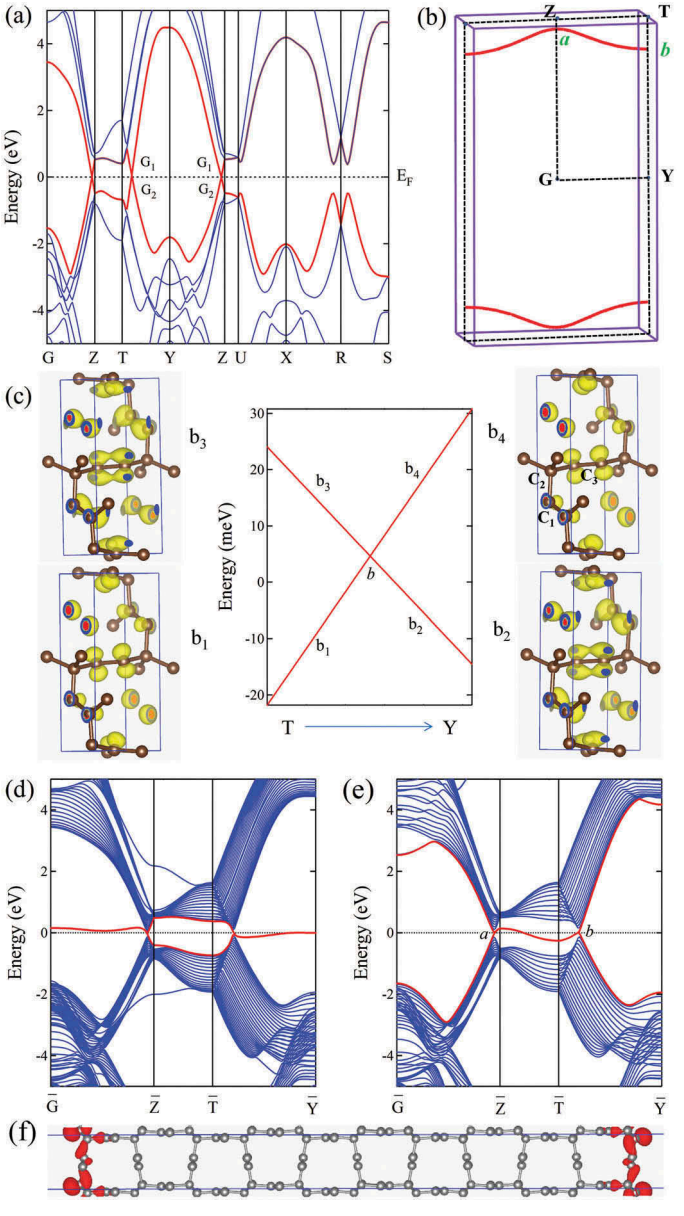

Figure 9. Calculated bulk and surface band structures of so-C_{12} at equilibrium lattice parameters. (a) The bulk band structure along several high-symmetry directions. G_1 and G_2 indicate the irreducible representations of the two crossing bands, respectively. (b) The BZ with several high-symmetry momenta indicated, and the nodal lines (red), formed by the band crossing points, in the G-Z-T-Y mirror plane. The *a* and *b* points represent the nodal point located along G-Z and T-Y line, respectively. (c) The band-decomposed charge density isosurfaces (0.07 e/Å^3) around the nodal point *b* along T-Y direction in BZ. (d,e) The (010) surface states obtained using a ten-layer-thick slab geometry along the [010] direction. The surface flat band (red line) can be inside or outside the surface projected nodal lines, depending on the termination of the surface without (d) or with (e) saturation by hydrogen atoms. The projected surface BZ $\bar{G}$-$\bar{Z}$-$\bar{T}$-$\bar{Y}$ is marked relative to G-Z-T-Y in bulk in (b). (f) Partial charge density isosurfaces (0.05 e/Å^3) related to the (red) surface bands in (d) at the $\bar{G}$ point. The outermost atoms are C_2 and C_3 with dangling bonds on C_2 sites.

Figure 9(d)] of two symmetric (up and down) nodal lines, depending on the termination of the surface with or without saturation by hydrogen atoms. In the Figure 9(f) the partial charge density isosurfaces related to the energy bands around the Fermi level in Figure 9(d) at $\bar{G}$ point are plotted. The electronic charges are located on the topmost surface carbon layers, confirming that the surface flat band is indeed deriving from the surface atoms.

As a topological nodal line semimetal, the nodal line structure is usually protected by the topological invariant, *i.e.* the Berry phase (a $\mathbb{Z}_2$-type invariant) along a closed path encircling the nodal line [69]. To clarify this point, we have calculated the Berry phase using the Wannier Tools package [88] based on a Wannier tight-binding model constructed by Wannier90 [89]. The Berry phase with a closed loop surrounding the nodal lines [see Figure 10(a)] is calculated to be π. Further, the Berry phase (or Zak phase) along the line passing through the BZ parallel to the k_y axis are calculated. If the line is inside the area between two separated nodal lines [see Figure 10(b)], the result is either 0 or π. The nonzero quantized Berry phase further confirms the nodal-line feature in so-C_{12} carbon. The appearance of surface states at the surface of nodal line semimetal arises from a quantized Berry phase. Since the Berry phase is equal to π for any closed path that interlinks with the nodal line, the surface states should connect the *a* and *b* points on the projected nodal loop in the 2D momentum space in Figure 9(d,e) since the surface states and the nodal line in bulk are at the same energy level.

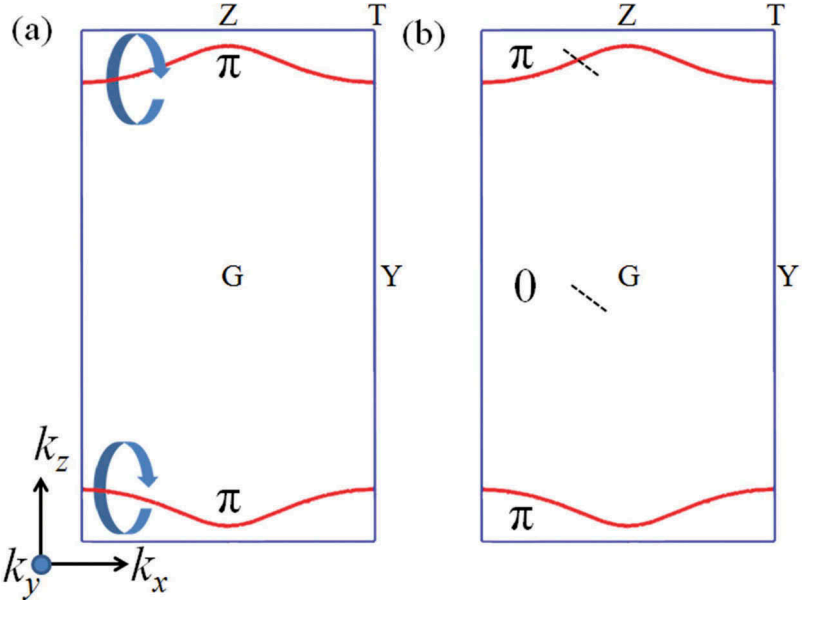

Figure 10. (a) Berry phase with a closed loop surrounding one of the nodal lines. (b) Berry phase using two lines (the black dash lines) in k_y direction passing through the BZ inside or outside between two separated nodal lines. The result is either 0 or π.

By carefully comparing the structure of so-C_{12} with that in ign-C_6 [60], mC16 [66], and bct-C_{12} [61], we found that the all these graphene network structures can be constructed by inserting zigzag carbon chains between the graphene layers in graphite. Specifically, the so-C_{12} is very similar to ign-C_6 with the similar crystal structures (so-C_{12} in D_{2h}^{11} and ign-C_6 in D_{2h}^{17} symmetry) and electronic band structures. The difference between these structures might be simply due to a slight difference in the stacking of graphene layers. To understand the reconstruction process and kinetics, the pathways from polymeric (3,3) CNT toward bct-C_{12} [61] and ign-C_6 [60] are also simulated at 10 GPa [67]. The enthalpy barriers are estimated to be 0.30 eV toward bct-C_{12} and 0.34 eV toward ign-C_6. These enthalpy barriers are larger than the values of $0.19-0.22$ eV for the pathway toward so-C_{12}. These results suggest that so-C_{12} is more preferred than bct-C_{12} and ign-C_6 based on kinetics [67].

4.2. Nodal nets comprising multiple-interconnected nodal lines in body-centered tetragonal C_{40}

The body-centered tetragonal C_{40} carbon allotrope can be constructed by inserting a benzene ring into each C-C bond in a previously established all-sp^3 bct-C_4 carbon lattice [9]. The resulted sp^2-sp^3 interconnected graphene network structure contains fourty atoms in one unit cell, thus termed bct-C_{40}. Electronic band structure calculations reveal that bct-C_{40} belongs to a new class of topological nodal net semimetal that exhibits nodal nets comprising multiple interconnected nodal lines in bulk and have two coupled drumhead-like flat bands around the Fermi level on its surface [68].

Figure 11(a) shows the body-centered tetragonal network structure of bct-C_{40} in $I4/mmm$ (D_{4h}^{17}, No. 139) symmetry. The calculated equilibrium lattice parameters are a = 12.901 Å and c = 2.46 Å with three inequivalent crystallographic sites C_1, C_2 and C_3, occupying the 8h (0.7257, 0.7257, 0.5), 16l_1 (0.7370, 0.6096, 0.5), and 16l_2 (0.7615, 0.0558, 0.5) Wyckoff positions, respectively. The carbon atoms on the 16l_1 and 16l_2 sites form eight benzene rings with aromatic sp^2 hybridization, while the carbon atoms on the 8h sites form four zigzag carbon chains as in bct-C_4 [9]. There are two sets of distinct C-C bonds in this structure, namely two sp^3 single longer bonds of 1.516 Å (C_1-C_1) and 1.505 Å (C_1-C_2), and two shorter sp^2 aromatic bonds of 1.412 Å (C_2-C_3) and 1.440 Å (C_3-C_3). There are also two sets of distinct bond angles: 109.49^o for $\angle C_1$-C_1-C_1, 111.80^o for $\angle C_1$-C_1-C_2, and 101.09^o for $\angle C_2$-C_1-C_2, which are close to the 109.5^o angle in diamond; 119.37^o for $\angle C_1$-C_2-C_3, 121.11^o for $\angle C_3$-C_2-C_3, and 119.43^o for $\angle C_3$-C_3-C_2, which are close to the 120^o angle in graphene. Note that bct-C_{40} has a 20-atom primitive cell [see Figure 11(b)], and it can be regarded as a crystalline modification of (5,5) CNT [31].

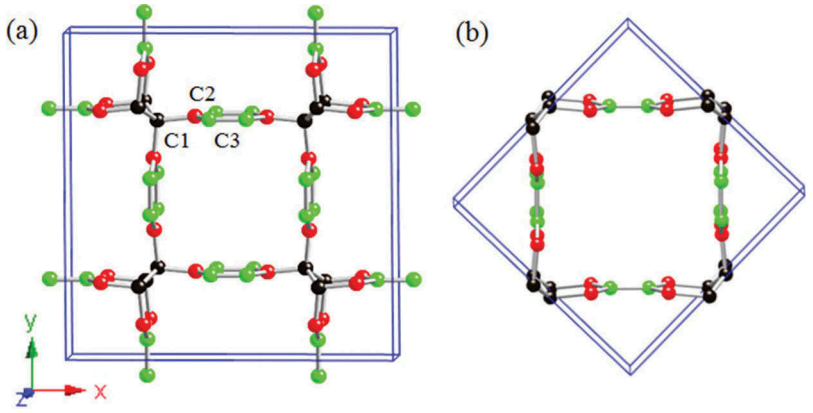

Figure 11. (a) The 40-atom unit cell of bct-C_{40} with lattice parameters a = 12.9012 Å, c = 2.4599 Å, occupying the 8*h* (0.7257, 0.7257, 0.5), 16l_1 (0.7370, 0.6096, 0.5), and 16l_2 (0.7615, 0.0558, 0.5) Wyckoff positions denoted by C_1, C_2 and C_3, respectively. (b) A 20-atom primitive cell of bct-C_{40} viewed as a crystalline modification of the (5,5) CNT.

Figure 12 show the calculated bulk and surface band structures of bct-C_{40}. It is found that bct-C_{40} has interconnected nodal lines forming two nearly 2D nodal nets in BZ [Figure 12(c)], which is distinct from all existing, both nodal point and nodal line, topological semimetals shown above [90]. The crossing bands forming these nodal lines belong to two different irreducible representations G_1 and G_2 [Figure 12(a)] distinguished by opposite mirror eigenvalues. The resulted nodal lines go through the whole BZ instead of forming a closed ring found in all-sp^2 carbon network structures [59,62,64]. They are topologically robust protected by the coexisting time-reversal and inversion symmetries without considering the spin-orbit coupling [59] and are constrained on the mirror planes [91]. The nodal lines form two boxed-asterisk shaped nets and the connecting points are on the intersecting lines of different mirror planes.

Note that the nodal nets discussed by Bzdusek *et al.* in [92] are different from bct-C_{40} in the following aspects: (1) the nodal net in bct-C_{40} is formed by type-B nodal lines going through the whole BZ, while that in the work by Bzdusek *et al.* is formed by type-A nodal rings traversing only part of the BZ; (2) in bct-C_{40}, nonsymmorphic symmetry is not required but inversion symmetry is necessary, while in the work by Bzdusek *et al.* more than one glide mirrors and noncentrosymmetric symmetry are needed; (3) the nodal net in bct-C_{40} is nearly 2D, rather than 3D reported by Bzdusek *et al.*; (4) in bct-C_{40}, the mirror symmetry constrains the nodal lines inside the mirror plane but its existence is topologically protected by inversion, time-reversal and spin rotation symmetries. Therefore, the crossing points of different nodal lines naturally appear on the intersection lines of different mirror planes. However, in the work by Bzdusek *et al.*, the nodal lines must appear on the glide mirror plane, which also constrains the location of the tangent point of the two nodal rings.

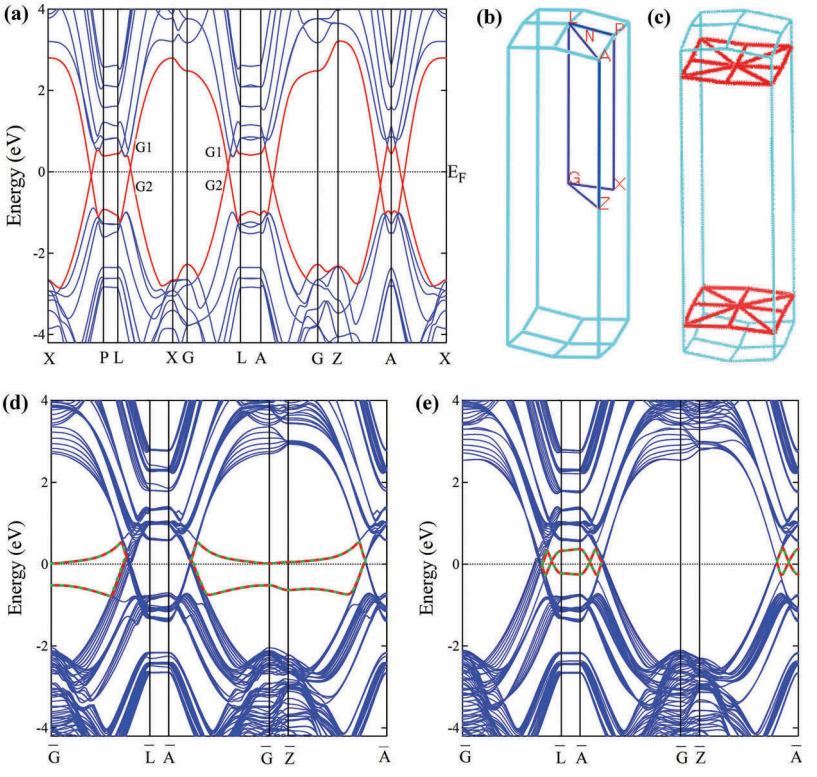

Figure 12. Calculated bulk and surface band structures of bct-C_{40}. (a) The bulk band structure along several high-symmetry directions. G_1 and G_2 indicate the irreducible representations of the two crossing bands, respectively. (b) The bulk BZ with several high-symmetry points indicated at G(0.00, 0.00, 0.00); X(0.00, 0.00, 0.50); P(0.25, 0.25, 0.25); N(0.00, 0.50, 0.00); Z (−0.50, 0.50, 0.50); L(0.26, 0.26, −0.26), and A(−0.26, 0.74, 0.26). (c) Two symmetric-boxed-asterisk shaped nodal nets (red lines) formed by several nodal lines is in the high symmetric mirror plane. (d) and (e) show the (100) surface band states. In (e), the surface dangling bonds are saturated with hydrogen atoms. There are two coupled surface flat bands with one occupied and the other unoccupied around the Fermi level.

Figure 12(d) and 12(e) show the calculated (100) surface states of bct-C_{40} using a slab geometry along the [93] crystalline direction, where the surface dangling bonds are saturated with hydrogen atoms in Figure 12(e). The top and bottom surface bands are marked in red solid and green dotted lines, respectively. They are degenerate due to the inversion symmetric slab model used in the calculation. The surface bands can be inside (region containing the $\bar{G}$ point) or outside (region containing the BZ boundaries) of the momentum space divided by the two symmetric nodal nets depending on the details of the surface termination. When the surface dangling bonds are (not) saturated with hydrogen atoms, the surface bands are outside (inside), which are similar to the results obtained in other nodal line systems [62]. A distinct property of bct-C_{40} is that it hosts two surface flat bands, which is different from the previously proposed nodal line semimetals with only a single flat surface band inside or outside the

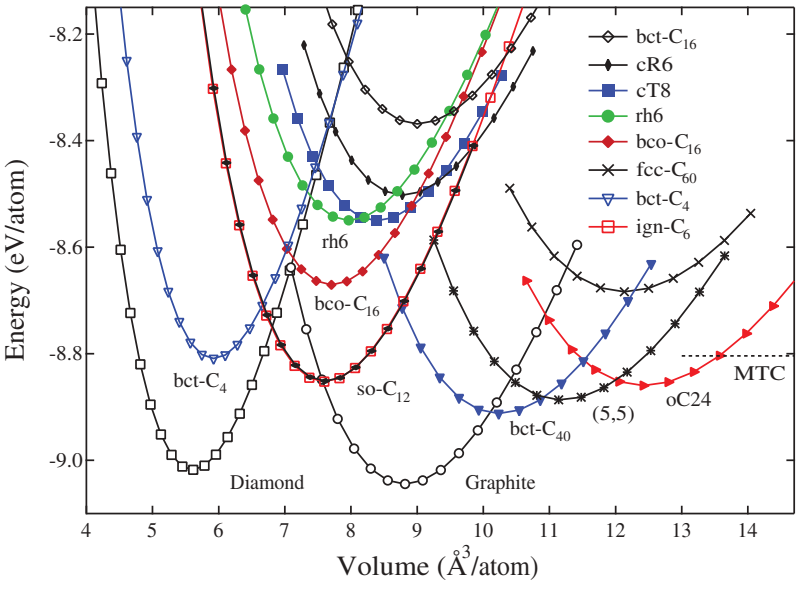

Figure 13. Calculated energy versus volume per atom for various carbon allotropes in all-sp^2 or mixed sp^2-sp^3 bonding networks. The detailed structures are described in text.

projected nodal line or ring [58–64]. Similar surface states were also found on the (110) surface of bct-C_{40} [68]. This distinct property is due to the superposition of the projection regions from the multiple nodal lines in the nodal net. Recently, Bzdusek *et al.* [92] and Hyart *et al.* [94] have studied this situation and found that it is possible to have multiple zero-energy flat surface bands if chiral symmetry is assumed. In the case of bct-C_{40}, the chiral symmetry is absent, and the coupling of the two surface states opens a gap with two bands located below and above the Fermi level, respectively. This finding provides a multiband rather than a single-band-based flat-band platform to study possible novel-correlated effects.

5. Relative stability for the new carbon allotropes

Finally, we discuss the relative structural stability. The total energies are calculated using the density functional theory as implemented in the Vienna *ab initio* simulation package (VASP) [95]. The generalized gradient approximation (GGA) developed by Armiento-Mattsson (AM05) [96] was adopted for the exchange-correlation function for the structural relaxation. The all-electron projector augmented wave (PAW) method [97] was adopted with $2s^2 2p^2$ treated as valence electrons. A plane-wave basis set with a large energy cutoff of 800 eV was used. Convergence criteria employed for both the electronic self-consistent relaxation and the ionic relaxation were set to 10^{-8} eV and 0.01 eV/Å for energy and force, respectively. The electronic band structures and related properties are obtained using the standard GGA-PBE method [98], while the band gaps are

Table 1. Calculated equilibrium structural parameters (space group, volume V_0, total energy E_{tot}, bulk modulus B_0, and HSE06 electronic band gap E_g for MTC [59], bco-C_{16} [62], bct-C_{16} [64], ign-C_6 [60], oC24 [65], so-C_{12} [67] and bct-C_{40} [68] in all-sp^2 or sp^2-sp^3 hybrid networks compared to diamond, and other all-sp^2 carbon phases including graphite, fcc-C_{60} [81], and three chiral framework structures cR6 [2], cT8 [2], rh6 [6] at zero pressure, compared to available experimental data [4].

Structure	Method	V_0(Å^3)	E_{tot} (eV)	B_0 (GPa)	E_g (eV)
Diamond ($Fd\bar{3}m$)	AM05	5.60	−9.018	451	5.36
	Exp [4]	5.67		446	5.47
cR6 ($R\bar{3}m$)	AM05	8.78	−8.502	268	2.95
cT8 ($I4_1/amd$)	AM05	8.40	−8.551	283	2.41
rh6 ($R\bar{3}m$)	AM05	7.96	−8.550	299	0.47
MTC ($Pm\bar{3}m$)	AM05	17.55	−8.804	138	semimetal
bco-C_{16} ($Imma$)	AM05	7.70	−8.671	315	semimetal
bct-C_{16} ($I4_1/amd$)	AM05	9.00	−8.369	257	semimetal
ign-C_6 ($Cmcm$)	AM05	7.60	−8.852	323	semimetal
oC24 ($Cmmm$)	AM05	12.43	−8.858	192	semimetal
so-C_{12} ($Pbcm$)	AM05	7.61	−8.851	322	semimetal
bct-C_{40} ($I4/mmm$)	AM05	10.23	−8.912	239	semimetal
fcc-C_{60} ($Fm\bar{3}$)	AM05	12.14	−8.684	198	
Graphite ($P6_3/mmc$)	AM05	8.81	−9.045	280	
	Exp [4]	8.78		286	

corrected using a hybrid density functional based on the Heyd-Scuseria-Ernzerhof scheme (HSE06) [99]. The calculated equilibrium structural parameters, total energy, bulk modulus, and electronic band gap are list in Table 1.

Figure 13 shows the calculated total energy versus volume per atom for the nodal line semimetals in all-sp^2 or sp^2-sp^3 hybrid networks compared to the all-sp^3 bct-C_4 [9] and diamond, and other all-sp^2 carbon phases including graphite, fcc-C_{60} fullerene [81], and the recently reported chiral framework structures cR6 [2], cT8 [2] and rh6 carbon [6]. For all-sp^2 carbon phases, the MTC [59] is more stable than bco-C_{16} [62] and bct-C_{16} [64] with a large equilibrium volume of 17.55 Å^3/atom (see Table 1); the stability of bco-C_{16} is comparable to that of fcc-C_{60}, and more favorable than rh6 carbon phase with a substantial energy gain of 0.12 eV per carbon atom due to its complementary chirality [62]; Meanwhile, bct-C_{16} [64] is topologically corresponding to the 2D square lattice as well as cT8 [6], but it is less stable than cT8, due to the structure of bct-C_{16} is consisting of two eightfold handed chains with same chirality; On the other hand, for the sp^2-sp^3 hybrid network structures such as ign-C_6 [60], oC24 [65], so-C_{12} [67], and bct-C_{40} [68], they are all energetically stable comparable with (5,5)-CNT, and more favorable than C_{60}, bco-C_{16}, and the chiral framework structures cR6, cT8 [2] and rh6 carbon [6] in all-sp^2 bonding networks. Especially, bct-C_{40} is slightly (0.11∼0.13 eV/atom) higher in energy than diamond and graphite, but more stable than all the other carbon phases examined here.

6. Conclusions and outlook

As discussed through several examples in the preceding text, the all-sp^2 carbon network structures such as Mackay-Terrones carbon crystal [59], body-centered orthorhombic C_{16} [62], and a body-centered tetragonal C_{16}

[64], like to form type-A nodal rings that reside inside a mirror plane of the BZ, while the sp^2-sp^3 hybrid network structures such as interpenetrated graphene network C_6 [60], orthorhombic oC24 [65], simple orthorhombic C_{12} [67], and body-centered tetragonal C_{40} [68], like to form type-B nodal lines that go through the whole BZ. Especially, body-centered tetragonal C_{40} belongs to a new class of topological nodal net semimetal that exhibits nodal nets comprising multiple-interconnected nodal lines in bulk and have two coupled drumhead-like flat bands around the Fermi level on its surface [68].

Beside these nodal lines or nodal net semimetals, the 3D Weyl-surface semimetals are also reported in triangular graphene network TGN(2,2) [93], quadrilateral graphene network QGN(2,2) [93], and hexagonal graphene network HGN(2,2) [93], respectively. Noted that such Weyl surfaces are closely related to an additional sublattice-symmetry operator in the tight-binding model [93], in contrast to the nodal nets reported in bct-C_{40} [68]. A similar Dirac surface was also reported in the high symmetric bct-C_{12} [61], but it should decay to type-B nodal lines in the low symmetric phase such as so-C_{12} reported here [67]. Recently, a new metastable 3D carbon allotrope entirely composed of pentagon rings [100] is also reported. The unique structure of this Pentagon carbon leads to extraordinary electronic properties, making it a cornucopia of emergent topological fermions. All of these results expand the realm of nodal manifolds in topological semimetals.

These carbons based topological nodal line semimetals can support topological surface flat bands, which are fascinating for generating new quantum states. For example, Kopnin *et al.* [80] have proposed to realize high-temperature superconductor by introducing pairing interaction into these flat bands. Chen *et al.* [101] proposed that if electron–electron interaction is taken into account, the surface flat bands will lead to Stoner ferromagnetic instability and even 2D Chern insulator at the surface. These expectation seems to be very promising since the recent remarkable experimental observation of Mott insulator and superconductor in twisted bilayer graphene. These have been widely believed to be related with flat bands that arises at a 'magic' twist angle [102,103].

Disclosure statement

No potential conflict of interest was reported by the authors.

Funding

This study was supported by the National Natural Science Foundation of China (Grants No. 11274356, No. 11674364 and No.11674369) and the Strategic Priority Research Program of the Chinese Academy of Sciences (Grants No. XDB28000000 and XXH13506-202). H. W. acknowledge the support from the National Key Research and Development Program of

China (Grants No. 2016YFA0300600 and 2018YFA0305700), the Science Challenge Project (TZ2016004), the K. C. Wong Education Foundation (GJTD-2018-01), the Beijing Natural Science Foundation (Z180008), and the Beijing Municipal Science and Technology Commission (Z181100004218001).

References

[1] Balaban AT. Carbon and its nets. Comput Math Applic. 1989;17:397–416.
[2] Wang JT, Chen CF, Kawazoe Y. New carbon allotropes with helical chains of complementary chirality connected by ethene-type π-conjugation. Sci Rep. 2013;3:03077.
[3] Belenkov EA, Greshnyakov VA. Classification of structural modifications of carbon. Phys Solid State. 2013;55:1754.
[4] Occelli F, Loubeyre P, Letoullec R. Properties of diamond under hydrostatic pressures up to 140 GPa. Nat Mater. 2003;2:151.
[5] Chalifoux WA, Tykwinski RR. Synthesis of polyynes to model the sp-carbon allotrope carbyne. Nat Chem. 2010;2:967.
[6] Wang JT, Chen CF, Wang EG, et al. A new carbon allotrope with six-fold helical chains in all-sp^2 bonding networks. Sci Rep. 2014;4:04339.
[7] Mao WL, Mao HK, Eng PJ, et al. Bonding changes in compressed superhard graphite. Science. 2003;302:425–427.
[8] Niu HY, Chen XQ, Wang SB, et al. Families of superhard crystalline carbon allotropes constructed via cold compression of graphite and nanotubes. Phys Rev Lett. 2012;108:135501.
[9] Umemoto K, Wentzcovitch RM, Saito S, et al. Body-centered tetragonal C_4: A viable sp^3 carbon allotrope. Phys Rev Lett. 2010;104:125504.
[10] Li Q, Ma YM, Oganov AR, et al. Superhard monoclinic polymorph of carbon. Phys Rev Lett. 2009;102:175506.
[11] Wang JT, Chen CF, Kawazoe Y. Low-temperature phase transformation from graphite to sp^3 orthorhombic carbon. Phys Rev Lett. 2011;106:075501.
[12] Wang JT, Chen CF, Kawazoe Y. Phase conversion from graphite toward a simple monoclinic sp^3-carbon allotrope. J Chem Phys. 2012;137:024502.
[13] Amsler M, Flores-Livas JA, Lehtovaara L, et al. Crystal structure of cold compressed graphite. Phys Rev Lett. 2012;108:065501.
[14] Zhao ZS, Tian F, Dong X, et al. Tetragonal allotrope of group 14 elements. J Am Chem Soc. 2012;134:12362.
[15] Selli D, Baburin IA, Martonak R, et al. Superhard sp^3 carbon allotropes with odd and even ring topologies. Phys Rev B. 2011;84:161411.
[16] Li ZZ, Lian CS, Xu J, et al. Computational prediction of body-centered cubic carbon in an all-sp^3 six-member ring configuration. Phys Rev B. 2015;91:214106.
[17] Iijima S. Helical microtubules of graphitic carbon. Nature. 1991;354:56–58.
[18] Kroto HW, Heath JR, O'brien SC, et al. C_{60}: Buckminsterfullerene.. Nature. 1985;318:162–163.
[19] Novoselov KS, Geim AK, Morozov SV, et al. Electric field effect in atomically thin carbon films. Science. 2004;306:666–669.
[20] Baughman RH, Eckhardt H, Kertesz M. Structure-property predictions for new planar forms of carbon: Layered phases containing sp^2 and sp atoms. J Chem Phys. 1987;87:6687–6699.
[21] Haley MM, Brand SC, Pak JJ. Carbon networks based on dehydrobenzoannulenes: synthesis of graphdiyne substructures. Angew Chem Int Ed Eng. 1997;36:836.

[22] Li G, Li Y, Liu H, et al. Architecture of graphdiyne nanoscale films. Chem Commun. 2010;46:3256–3258.
[23] Ivanovskii AL. Graphynes and graphdyines. Prog Sol State Chem. 2013;41:1–19.
[24] Kehoe JM, Kiley JH, English JJ, et al. Carbon networks based on dehydrobenzoannulenes. 3. Synthesis of graphyne substructures. Org Lett. 2000;2:969–972.
[25] Wang JT, Chen CF, Li HD, et al. Three-dimensional carbon allotropes comprising phenyl rings and acetylenic chains in sp+sp^2 hybrid networks. Sci Rep. 2016;6:24665.
[26] Hirsch A. The era of carbon allotropes. Nat Mater. 2010;9:868.
[27] Jo JY, Kim BG. Carbon allotropes with triple bond predicted by first-principle calculation: Triple bond modified diamond and T-carbon. Phys Rev B. 2012;86:075151.
[28] Huang L, Xiang Z, Cao D. A porous diamond carbon framework: a new carbon allotrope with extremely high gas adsorption and mechanical properties. J Mater Chem A. 2013;1:3851.
[29] Wang JT, Chen CF, Mizusekid H, et al. New carbon allotropes in sp+sp^3 bonding networks consisting of C_8 cubes.Phys Chem Chem Phys. 2018;20:7962.
[30] Karfunkel HR, Dresslert T. New hypothetical carbon allotropes of remarkable stability estimated by MNDO solid-state SCF computations. J Am Chem Soc. 1992;114:2285–2288.
[31] Kuc A, Seifert G. Hexagon-preserving carbon foams: properties of hypothetical carbon allotropes. Phys Rev B. 2006;74:214104.
[32] Zhao CX, Niu CY, Qin ZJ, et al. H18 carbon: a new metallic phase with sp^2-sp^3 hybridized bonding network. Sci Rep. 2016;6:21879.
[33] Klett JW, McMillan AD, Gallego NC, et al. The role of structure on the thermal properties of graphitic foams. J Mater Sci. 2004;39:3659–3676.
[34] Klett J, Hardy R, Romine E, et al. High-thermal-conductivity, mesophase-pitch-derived carbon foams: effect of precursor on structure and properties. Carbon. 2000;38:953–973.
[35] Krainyukova NV, Zubarev EN. Carbon honeycomb high capacity storage for gaseous and liquid species. Phys Rev Lett. 2016;116:055501.
[36] Ben T, Ren H, Ma SQ, et al. Targeted synthesis of a porous aromatic framework with high stability and exceptionally high surface area. Angew Chem, Int Ed. 2009;48:9457–9460.
[37] Armitage NP, Mele EJ, Vishwanath A. Weyl and Dirac semimetals in three-dimensional solids. Rev Mod Phys. 2018;90:15001.
[38] Burkov AA, Hook MD, Balents L. Topological nodal semimetals. Phys Rev B. 2011;84:235126.
[39] Phillips M, Aji V. Tunable line node semimetals. Phys Rev B. 2014;90:115111.
[40] Fang C, Chen Y, Kee HY, et al. Topological nodal line semimetals with and without spin-orbital coupling. Phys Rev B. 2015;92:081201.
[41] Kim Y, Wieder BJ, Kane CL, et al. Dirac line nodes in inversion-symmetric crystals. Phys Rev Lett. 2015;115:036806.
[42] Yu R, Weng H, Fang Z, et al. Topological node-line semimetal and Dirac semimetal state in antiperovskite Cu_3PdN. Phys Rev Lett. 2015;115:036807.
[43] Volovik GE. From standard model of particle physics to room-temperature superconductivity. Phys Scr. 2015;T164:014014.
[44] Heikkila TT, Volovik GE. Nexus and Dirac lines in topological materials. New J Phys. 2015;17:093019.
[45] Xie LS, Schoop LM, Seibel EM, et al. A new form of Ca_3P_2 with a ring of Dirac nodes.APL Mater. 2015;3:083602.

[46] Chan YH, Chiu CK, Chou MY, et al. Ca_3P_2 and other topological semimetals with line nodes and drumhead surface states. Phys Rev B. 2016;93:205132.
[47] Yan Z, Wang Z. Tunable weyl points in periodically driven nodal line semimetals. Phys Rev Lett. 2016;117:087402.
[48] Chan CK, Oh YT, Han JH, et al. Type-II Weyl cone transitions in driven semimetals. Phys Rev B. 2016;94:121106.
[49] Bian G, Chang TR, Sankar R, et al. Topological nodal-line fermions in spin-orbit metal PbTaSe2. Nat Commun. 2016;7:10556.
[50] Zhang CL, Yuan ZJ, Bian G, et al. Superconducting properties in single crystals of the topological nodal semimetal $PbTaSe_2$. Phys Rev B. 2016;93:054520.
[51] Zhang XM, Yu ZM, Sheng XL, et al. Coexistence of four-band nodal rings and triply degenerate nodal points in centrosymmetric metal diborides. Phys Rev B. 2017;95:235116.
[52] Wang Z, Sun Y, Chen XQ, et al. Dirac semimetal and topological phase transitions in A_3Bi (A = Na, K, Rb). Phys Rev B. 2012;85:195320.
[53] Zhao JZ, Yu R, Weng H, et al. Topological node-line semimetal in compressed black phosphorus. Phys Rev B. 2016;94:195104.
[54] Liang QF, Zhou J, Yu R, et al. Node-surface and node-line fermions from nonsymmorphic lattice symmetries. Phys Rev B. 2016;93:085427.
[55] Huang H, Liu J, Vanderbilt D, et al. Topological nodal-line semimetals in alkaline-earth stannides, germanides, and silicides. Phys Rev B. 2016;93:201114.
[56] Ronghan L, Hui M, Cheng X, et al. Dirac node lines in pure alkali earth metals. Phys Rev Lett. 2016;117:096401.
[57] Hirayama M, Okugawa R, Miyake T, et al. Topological Dirac nodal lines and surface charges in fcc alkaline earth metals. Nat Commun. 2017;8:14022.
[58] Mikitik GP, Sharlai YV. Band-contact lines in the electron energy spectrum of graphite. Phys Rev B. 2006;73:235112.
[59] Weng H, Liang Y, Xu Q, et al. Topological node-line semimetal in three-dimensional graphene networks. Phys Rev B. 2015;92:045108.
[60] Chen Y, Xie Y, Yang SA, et al. Nanostructured carbon allotropes with weyl-like loops and points. Nano Lett. 2015;15:6974–6978.
[61] Dong X, Hu M, He JL, et al. A new phase from compression of carbon nanotubes with anisotropic Dirac fermions. Sci Rep. 2015;5:10713.
[62] Wang JT, Weng H, Nie S, et al. Body-centered orthorhombic C_{16}: A novel topological node-line semimetal. Phys Rev Lett. 2016;116:195501.
[63] Cheng Y, Du J, Melnik R, et al. Novel three dimensional topological nodal line semimetallic carbon. Carbon. 2016;98:468–473.
[64] Cheng Y, Feng X, Cao XT, et al. Body-centered tetragonal C_{16}: A novel topological node-line semimetallic carbon composed of tetrarings. Small. 2017; 13:1602894.
[65] Li ZZ, Chen J, Nie SM, et al. Orthorhombic carbon oC24: A novel topological nodal line semimetal. Carbon. 2018;133:39–43.
[66] Feng X, Wu QS, Cheng Y, et al. Monoclinic C_{16}: sp^2-sp^3 hybridized nodal-line semimetal protected by PT-symmetry.Carbon. 2018;127:527–532.
[67] Wang JT, Chen CF, Kawazoe Y. Topological nodal line semimetal in an orthorhombic graphene network structure. Phys Rev B. 2018;97:245147.
[68] Wang JT, Nie SM, Weng H, et al. Topological nodal-net semimetal in a graphene network structure. Phys Rev Lett. 2018;120:026402.
[69] Hyart T, Ojajärvi R, Heikkilä TT. Two topologically distinct dirac-line semimetal phases and topological phase transitions in rhombohedrally stacked honeycomb lattices. J Low Temp Phys. 2018;191:35–48.

[70] Neto AC, Guinea F, Peres N, et al. The electronic properties of graphene. Rev Mod Phys. 2009;81:109.
[71] Balandin AA, Ghosh S, Bao W, et al. Superior thermal conductivity of single-layer graphene. Nano Lett. 2008;8:902-907.
[72] Lee C, Wei X, Kysar JW, et al. Measurement of the elastic properties and intrinsic strength of monolayer graphene. Science. 2008;321:385–388.
[73] Geim AK. Graphene: status and prospects. Science. 2009;324:1530–1534.
[74] Novoselov KS, Geim AK, Morozov SV, et al. Two-dimensional gas of massless Dirac fermions in graphene. Nature. 2005;438:197–200.
[75] Naumis GG, Barraza-Lopez S, Oliva-Leyva M, et al. Electronic and optical properties of strained graphene and other strained 2D materials: a review. Rep Prog Phys. 2017;80:096501.
[76] Malko D, Neiss C, Viñes F, et al. Competition for graphene: graphynes with direction-dependent dirac cones. Phys Rev Lett. 2012;108:086804.
[77] Tagami M, Liang Y, Naito H, et al. Negatively curved cubic carbon crystals with octahedral symmetry. Carbon. 2014;76:266–274.
[78] Qi XL, Zhang SC. Topological insulators and superconductors. Rev Mod Phys. 2011;83:1057.
[79] Ito Y, Tanabe Y, Qiu HJ, et al. High-quality three-dimensional nanoporous graphene. Ang Chem. 2014;126:4922.
[80] Kopnin NB, Heikkila TT, Volovik GE. High-temperature surface superconductivity in topological flat-band systems. Phys Rev B. 2011;83:220503.
[81] David WIF, Ibberson RM, Matthewman JC, et al. Crystal structure and bonding of ordered C_{60}. Nature. 1991;353:147–149.
[82] Chen PW, Huang FL, Yun SR. Characterization of the condensed carbon in detonation soot. Carbon. 2003;41:2093–2099.
[83] Pantea D, Brochu S, Thiboutot S, et al. A morphological investigation of soot produced by the detonation of munitions. Chemosphere. 2006;65:821–831.
[84] Vereshchagin AL, Yur'ev GS. Structure of detonation diamond nanoparticles. Inorg Mater. 2003;39:312–318.
[85] Wang JT, Chen CF, Wang DS, et al. Phase stability of carbon clathrates at high pressure. J Appl Phys. 2010;107:063507.
[86] Lian CS, Wang JT. Three-dimensional polymeric structures of single-wall carbon nanotubes. J Chem Phys. 2014;140:204709.
[87] The polymeric (3,3) CNT in Figure 8(a) contains two (3,3) CNTs in Imma symmetry. The lattice parameters are a = 8.536 Å, b = 2.485 Å, and c = 9.025 Å, occupying the 8i (0.4216, 0.25. 0.2341), 8i (0.1979, 0.25, 0.5374), and 8i (0.1711, 0.25, 0.7057) Wyckoff positions. It is a semicondutor with a direct band gap of 0.32 eV at the R point of the Brillouin zone.
[88] Wu QS, Zhang SN, Song HF, et al. WannierTools: an open-source software package for novel topological materials. Comput Phys Commun. 2018;224:405–416.
[89] Mostofi AA, Yates JR, Lee YS, et al. Wannier90: A tool for obtaining maximally-localised Wannier functions. Comput Phys Commun. 2008;178:685–699.
[90] Weng H, Dai X, Fang Z. Topological semimetals predicted from first-principles calculations. J Phys Condens Matter. 2016;28:303001.
[91] Fang C, Weng H, Dai X, et al. Topological nodal line semimetals. Chin Phys B. 2016;25:117106.
[92] Bzdusek T, Wu Q, Ruegg A, et al.Nodal-chain metals. Nature. 2016;538:75–78.
[93] Zhong CY, Chen YP, Xie Y, et al. Towards three-dimensional Weyl-surface semimetals in graphene networks. Nanoscale. 2016;8:7232–7239.

[94] Hyart T, Heikkila TT. Momentum-space structure of surface states in a topological semimetal with a nexus point of Dirac lines. Phys Rev B. 2016;93:235147.
[95] Kresse G, Furthmüller. Efficient iterative schemes for ab initio total-energy calculations using a plane-wave basis set. Phys Rev B. 1996;54:11169.
[96] Armiento R, Mattsson AE. Functional designed to include surface effects in self-consistent density functional theory. Phys Rev B. 2005;72:085108.
[97] Blöchl PE. Projector augmented-wave method. Phys Rev B. 1994;50:17953.
[98] Perdew JP, Burke K, Ernzerhof M. Generalized gradient approximation made simple. Phys Rev Lett. 1996;77:3865.
[99] Heyd J, Scuseria GE, Ernzerhof M. Hybrid functionals based on a screened coulomb potential. J Chem Phys. 2006;124:219906.
[100] Zhong CY, Chen YP, Yu ZM, et al. Three-dimensional pentagon carbon with a genesis of emergent fermions. Nat Commun. 2017;8:15641.
[101] Chen W, Lado JL. Interaction-driven surface Chern insulator in nodal line semimetals. Phys Rev Lett. 2019;122:016803.
[102] Cao Y, Fatemi V, Fang S, et al. Correlated insulator behaviour at Half-filling in magic-angle graphene superlattices. Nature. 2018;556:80-84.
[103] Cao Y, Fatemi V, Demir A, et al. Unconventional superconductivity in magic-angle graphene superlattices.Nature. 2018;556:43-50.